SCIENCE CHINA
Life Sciences

•RESEARCH PAPER•

https://doi.org/10.1007/s11427-021-1976-0

Ferritin nanocages for early theranostics of tumors via inflammation-enhanced active targeting

Bing Jiang[1,2†], Xiaohua Jia[3†], Tianjiao Ji[4,5], Meng Zhou[2], Jiuyang He[2], Kun Wang[3], Jie Tian[3,6*], Xiyun Yan[1,2*] & Kelong Fan[1,2*]

[1]*Nanozyme Medical Center, School of Basic Medical Sciences, Zhengzhou University, Zhengzhou 450001, China;*
[2]*CAS Engineering Laboratory for Nanozyme, Key Laboratory of Protein and Peptide Pharmaceuticals, Institute of Biophysics, Chinese Academy of Sciences, Beijing 100101, China;*
[3]*Key Laboratory of Molecular Imaging of Chinese Academy of Sciences, Institute of Automation, Chinese Academy of Sciences, Beijing 100190, China;*
[4]*CAS Key Laboratory for Biomedical Effects of Nanomaterials & Nanosafety, CAS Center for Excellence in Nanoscience, National Center for Nanoscience and Technology, Beijing 100190, China;*
[5]*Center of Materials Science and Optoelectronics Engineering, University of Chinese Academy of Sciences, Beijing 100049, China;*
[6]*Beijing Advanced Innovation Center for Big Data-Based Precision Medicine, School of Medicine, Beihang University, Beijing 100191, China*

Received April 13, 2021; accepted July 2, 2021; published online August 31, 2021

Engineered nanocarriers have been widely developed for tumor theranostics. However, the delivery of imaging probes or therapeutic drugs to the tumor pre-formation site for early and accurate detection and therapy remains a major challenge. Here, by using tailor-functionalized human H-ferritin (HFn), we developed a triple-modality nanoprobe IRdye800-M-HFn and achieved the early imaging of tumor cells before the formation of solid tumor tissues. Then, we developed an HFn-doxorubicin (Dox) drug delivery system by loading Dox into the HFn protein cage and achieved early-stage tumor therapy. The intravenous injection of HFn nanoprobes enabled the imaging of tumor cells as early as two days after tumor implantation, and the triple-modality imaging techniques, namely, near-infrared fluorescence molecular imaging (NIR-FMI), magnetic resonance imaging (MRI), and photoacoustic imaging (PAI), ensured the accuracy of detection. Further exploration indicated that HFn could specifically penetrate into pre-solid tumor sites by tumor-associated inflammation-mediated blood vessel leakage, followed by effective accumulation in tumor cells by the specific targeting property of HFn to transferrin receptor 1. Thus, the HFn-Dox drug delivery system delivered Dox into the tumor pre-formation site and effectively killed tumor cells at early stage. IRDye800-M-HFn nanoprobes and HFn-Dox provide promising strategies for early-stage tumor diagnosis and constructive implications for early-stage tumor treatment.

ferritin nanocage, early theranostics, tumor-associated inflammation, multimodality tumor imaging, drug delivery

Citation: Jiang, B., Jia, X., Ji, T., Zhou, M., He, J., Wang, K., Tian, J., Yan, X., and Fan, K. (2021). Ferritin nanocages for early theranostics of tumors via inflammation-enhanced active targeting. Sci China Life Sci 64, https://doi.org/10.1007/s11427-021-1976-0

INTRODUCTION

Early detection provides opportunity for the early treatment of tumors, thus improving the survival rate of cancer patients (Smith et al., 2006). Although numerous engineered nanoprobes have been developed and exhibited effective imaging for tumor detection (Alexiou et al., 2015; Chinen et al., 2015), most of the targeting strategies are based on the enhanced permeability and retention (EPR) effect of tumor

†Contributed equally to this work
*Corresponding authors (Jie Tian, email: jie.tian@ia.ac.cn; Xiyun Yan, email: yanxy@ibp.ac.cn; Kelong Fan, email: fankelong@ibp.ac.cn)

blood vessels (tumor-mediated EPR effect) (Greish, 2010; Sun et al., 2014). However, tumor blood vessels only dramatically increase when a solid tumor tissue grows beyond a minimal size, whereas metastasis may have already occurred prior to or during this condition (Croci et al., 2014; Feng et al., 2013; Frangioni, 2008; Teicher, 2006). Thus, during the tumor pre-formation stage, nanoprobe imaging strategies based on the typical EPR effects may not meet the demand, given that tumor blood vessels are lacking. Thus, new targeting strategies need to be explored for early tumor detection at this stage.

Revisiting the tumor microenvironment in tumor formation and development, researchers thought that the inflammation promoted by tumor cells stimulates tumor initiation while creating a favorable microenvironment for tumor growth (Ben-Neriah and Karin, 2011). Recent studies have confirmed that tumor-associated inflammation recruits inflammatory cells penetrating blood vessels to gather around tumor cells (Ben-Neriah and Karin, 2011; Maru, 2016). Tumor cell/tissue-induced inflammation can produce endothelial gaps in the surrounding blood vessels, which allows the leakage of serum proteins, such as albumin (3 nm×8 nm) or coagulation factors, represented by fibrinogen (10–40 nm×3 nm), into the extravascular space (tumor cell region) (Lima and Monteiro, 2013; Maru, 2016). Thus, tumor-associated inflammation-mediated blood vessel leakage provides a new opportunity for nanoprobes or drug carriers with a certain size to target tumor cells at the early stage of tumor formation, thereby realizing tumor pre-formation detection and early therapy.

Imaging techniques provide important tools for tumor diagnosis. However, single-mode imaging techniques such as recent clinical X-rays, computed tomography, endoscopy, and ultrasound may lack accuracy for the detection of early-stage tumors, and have a low sensitivity that limits their capability to distinguish malignant lesions from benign ones. Multimodality imaging methods, combining the advantages of each imaging modality, may improve the accuracy of cancer detection (Thorsen et al., 2013; Xing et al., 2014). In a multimodality imaging strategy that integrates magnetic resonance imaging (MRI), near-infrared fluorescence molecular imaging (NIR-FMI), and photoacoustic imaging (PAI), MRI can provide high-contrast anatomical information, but it greatly suffers from limited spatial resolution (Kircher et al., 2012). NIR-FMI has high detecting sensitivity and real-time imaging capability, but it usually suffers from limited penetration depth due to the high absorption and scattering effect in tissues. As a hybrid imaging modality, PAI can overcome the imaging depth and resolution limits of NIR-FMI (Peng et al., 2016). Combining these imaging techniques may offer more comprehensive and precise information for the early detection of tumors.

An appropriate multimodality nanoprobe combining high specificity and sensitivity is essential to ensure the accuracy of early tumor detection (Chinen et al., 2015). In this study, human H-ferritin (HFn) was selected as the basic structural motif of the multimodality nanoprobe. Ferritin is a spherical iron storage protein composed of a self-assembled 24-subunit protein shell with an outer diameter of 12 nm and an interior cavity diameter of 8 nm (Fan et al., 2013); it contains multiple active groups that are modifiable in the cavity and external surface (Falvo et al., 2013; He et al., 2019; Jiang et al., 2019a; Jiang et al., 2019b; Li et al., 2012; Uchida et al., 2006; Wang et al., 2021; Zhang et al., 2021). Most importantly, HFn can specifically target tumor cells via an overexpressed tumor biomarker transferrin receptor 1 (TfR1) (Fan et al., 2012; Fan et al., 2018; Fan et al., 2017; Jiang et al., 2020; Li et al., 2010) without additional modifications of extra targeting ligands (Fan et al., 2012; Liang et al., 2014; Zhao et al., 2016). Theoretically, as a natural serum protein (Wang et al., 2010) with a proper size of 12 nm, ferritin can pass through the endothelial barrier of vascular vessels via inflammation-mediated blood vessel leakage. In addition, the 8 nm diameter cavity of HFn nanocage ensures the encapsulation of a great number of chemotherapeutic drugs into its protein nanocage, rendering ferritin a potential drug nanocarrier for tumor therapy (Fan et al., 2013; He et al., 2019; Jiang et al., 2020; Liang et al., 2014). Based on these unique characteristics, HFn is a potential biomaterial for the construction of nanoprobes and drug carriers for early-stage tumor imaging and therapy.

RESULTS AND DISCUSSION

Synthesis and characterization of IRdye800-M-HFn nanoprobes

We constructed an HFn nanoprobe IRdye800-M-HFn with triple-modality imaging techniques (NIR-FMI, PAI, and MRI) to target and image tumor cells at the early stage. IRdye800-M-HFn combined with NIR-FMI, MRI, and PA imaging modules realized high-sensitive fluorescence imaging, tissue and structure imaging, and PA-based deep-tissue high-resolution imaging and oxygen saturation imaging, thus providing a comprehensive assessment of tumor development.

Taking advantage of the unique protein nanocage architecture of human HFn, we bio-mimetically synthesized highly crystalline iron oxide nanoparticles within the interior cavity of HFn and labeled the protein shell with IRdye800 for tumor NIR-FMI/PAI/MRI triple-modality imaging (Figure 1A). The human HFn nanoparticles were recombinantly expressed in *E. coli* and purified as we previously reported (Fan et al., 2012; Liang et al., 2014). A total of 24 HFn subunits self-assembled into a spherical protein nanocage, with inner and outer diameters of 8 and 12 nm, respectively.

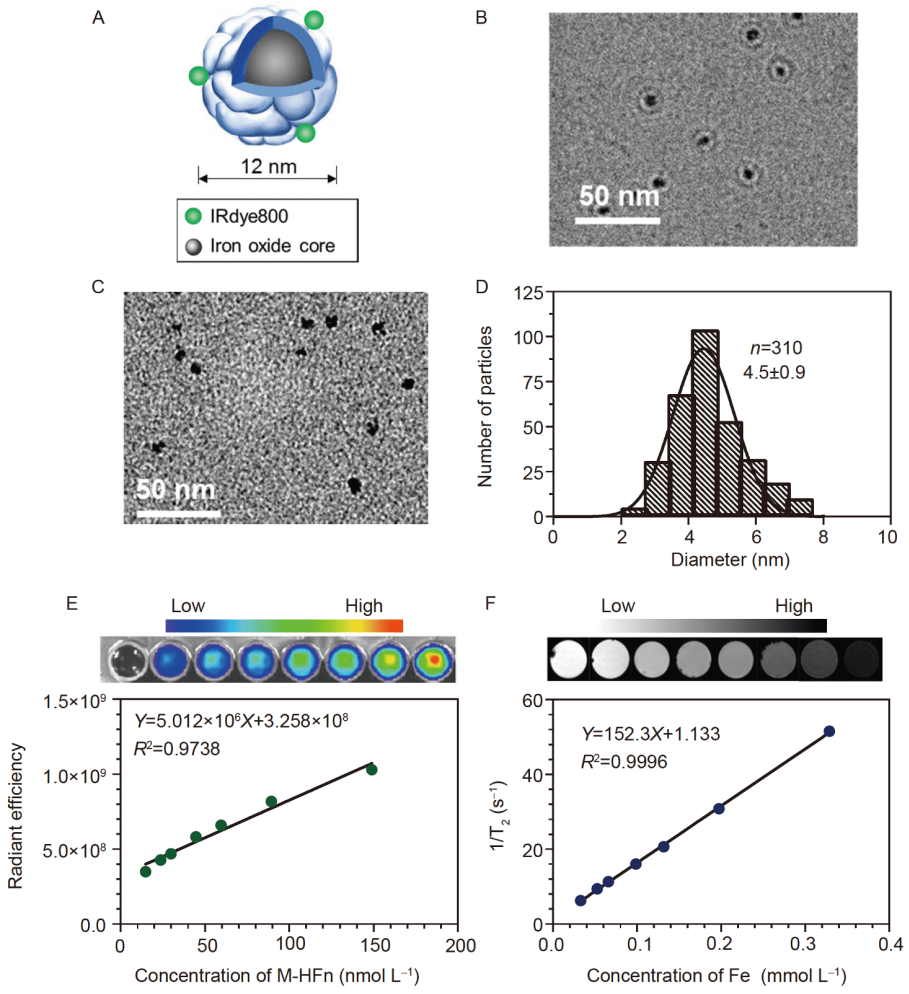

Figure 1 Preparation and characterization of IRdye800-M-HFn nanoprobes. A, Schematic of IRdye800-M-HFn nanoprobes. B, Cryo-EM images of IRdye800-M-HFn nanoprobes. C, TEM images of iron oxide cores of IRdye800-M-HFn nanoprobes. D, Size distribution of iron oxide cores of IRdye800-M-HFn nanoprobes, with a median diameter of 4.5 nm±0.9 nm. E and F, NIR-FMI images (E) and T_2-weighted MR images (F) of IRdye800-M-HFn nanoprobes at different concentrations.

Employing HFn nanocage as the nanoreactor, we synthesized magnetoferritin (M-HFn) nanoparticles via loading of Fe^{2+} into the cavities of HFn through hydrophilic channels in the protein shell, where iron oxide nanoparticles within the cavity were formed by using H_2O_2 as an oxidizing agent (Fan et al., 2012). We further labeled M-HFn nanoparticles with dye IRdye800 to form IRdye800-M-HFn triple-modality imaging nanoprobes. After purification, the IRdye800-M-HFn nanoprobes were analyzed by cryo-electron microscopy (Cryo-EM) and transmission electron microscopy (TEM). The protein shells of IRdye800-M-HFn had a well-defined morphology and were monodispersed in size (Figure 1B). Uniformly distributed iron oxide nanoparticles with an average diameter of 4.5 nm±0.9 nm were synthesized within the cavity of HFn nanocages (Figure 1C and D). The fluorescence intensity of nanoprobes confirmed the effective conjugation of IRdye800 to the protein shell (IRdye800:M-HFn=13:1) (Figure 1E). The MR contrast properties of M-HFn nanoprobes were determined at a 7.0-T magnetic field based on the iron concentrations of M-HFn, and the calculated relaxivity rate ($1/T_2$) was r_2=152.3±1.363 mM^{-1} s^{-1} (Figure 1F). The superparamagnetism of M-HFn nanoprobes renders them as potential contrast agents for MRI in tumor diagnosis (Uchida et al., 2008; Zhao et al., 2016).

Specific binding capability of M-HFn to TfR1-positive tumor cells

To evaluate the feasibility of HFn-based nanoprobes for early tumor detection, we selected a TfR1 high-expressing hepatocellular carcinoma (HCC) cell line (HepG2) for further research and the TfR1 low-expressing human breast cancer cell line MX-1 used as a negative control. The Western blot results confirmed the high expression of TfR1 in HepG2 cells, whereas MX-1 cells showed no evident TfR1 expression (Figure 2A). Anti-TfR1 monoclonal antibody specifi-

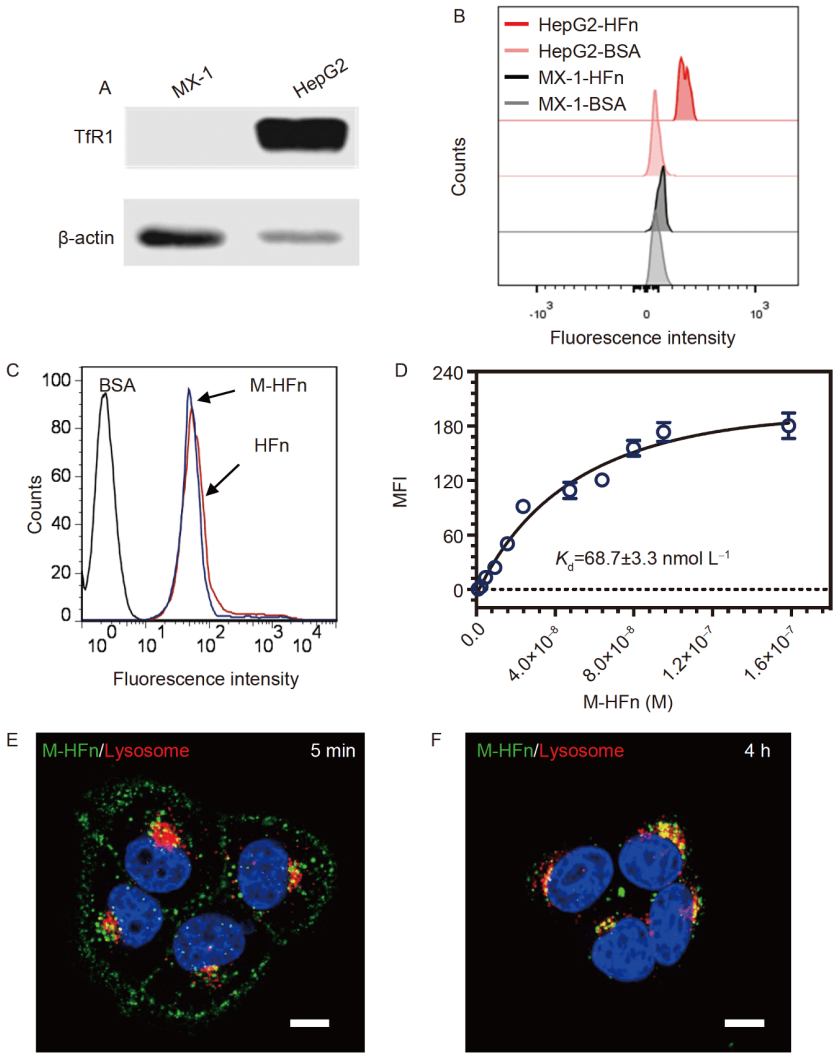

Figure 2 M-HFn nanoprobes specifically bound to TfR1 molecule on HCC cells via TfR1. A, Western blot of TfR1 expression in MX-1 cells and HepG2 cells. B, Flow cytometric analysis of the binding capability of HFn to HepG2 cells and MX-1 cells. C, Flow cytometric analysis of the specific binding of HFn and M-HFn nanoprobes to HepG2 cells. (D) The binding affinity (K_d) of M-HFn nanoprobe to TfR1 on HCC cells was 68.7 nmol L^{-1}±3.3 nmol L^{-1}. E and F, Confocal images of the intracellular uptake of M-HFn nanoprobes into HepG2 cells. At 5 min, most of the M-HFn nanoprobes were bound to the TfR1 in the membrane of HepG2 cells (E). At 4 h, the M-HFn nanoprobes were internalized by TfR1-mediated endocytosis and localized in lysosomes (F). Scale bar=10 μm.

cally bound to HepG2 cells, which further confirmed the high expression of TfR1 in HepG2 cells (Figure S1 in Supporting Information). The flow cytometry results showed that HFn specifically bound to HepG2 but not to MX-1 cells (Figure 2B). To verify whether the process of loading iron oxide core affected the specific binding of HFn nanoprobes to live tumor cells, we performed flow cytometry on HepG2 cells incubated with M-HFn. The M-HFn nanoprobes specifically bound to HepG2 cells, similar to the HFn nanoprobes. Moreover, the binding affinity (K_d) of M-HFn to HCC tumor cells was 68.7 nmol L^{-1}±3.3 nmol L^{-1}, which is consistent with that of HFn nanoprobes (Fan et al., 2012) (Figure 2C and D). These results indicated that M-HFn, the biomineralized HFn, has the same tumor cell binding activity as the HFn nanoprobes.

TfR1 on the cell membrane can effectively mediate ligand internalization post interaction (Daniels et al., 2006a; Daniels et al., 2006b; Hopkins, 1983). This unique property of TfR1 might enable HFn to deliver high concentration of NIR-FMI/PAI/MRI probes into TfR1-positive tumors to achieve tumor triple-modality imaging with high sensitivity and specificity. To test this hypothesis, we incubated the M-HFn nanoprobes with HepG2 cells for fluorescence microscopy observation. The lysosomes of HepG2 cells were stained by the lysosomal marker lysosomal-associated membrane protein 1. As shown in Figure 2E, the M-HFn nanoprobes were bound to the surface of HepG2 cells rapidly after incubation. The nanoprobes were internalized and located in the cytoplasm and lysosomes, as shown by their co-localization with M-HFn. After incubation with the HepG2 cells for 4 h, the majority of M-HFn nanoprobes were concentrated in the lysosomes (Figure 2F). These results

demonstrate that the specific binding of M-HFn nanoprobes to HepG2 cells led to enriched endocytosis and the subsequent trafficking of M-HFn to lysosomes in tumor cells.

In vivo NIR-FMI of tumor cells by IRdye800-M-HFn at the pre-solid tumor stage

We next evaluated the feasibility of IRdye800-M-HFn triple-modality nanoprobes for imaging of HCC cells before the formation of solid tumor tissues *in vivo*. We used a xenograft HCC tumor model in which the luciferase-transfected HepG2 (HepG2-Luc) cells were implanted into the flanks of athymic nude mice subcutaneously. The tumor-bearing mice were divided into two groups: one group was used for the investigation of tumor growth and the other for tumor cell imaging. First, we monitored the size of implanted HCC tumor cells via collecting the *in vivo* bioluminescence (BL) signal produced by HepG2-Luc cells after the intraperitoneal injection of luciferin (n=3 for each time point). The intensities of BL signals in the tumor region (Figure 3A and B), which are enclosed in red dashed circles, exhibited a decreasing trend from day 1 (D1) to D11 after implantation and reached its minima on D11. The pathological analysis also showed that the TfR1 expression on the tumor decreased from D4 to D11 (Figure S2 in Supporting Information). However, after D11, tumor growth accelerated at the log phase, in which the size of tumor reached 300 mm^3 on D20. According to the tumor immune surveillance hypothesis (Swann and Smyth, 2007), D4 represents the elimination phase when tumor cells are under the immune surveillance, and tumor cells form a cluster at this pre-solid tumor stage; D11 represents the equilibrium phase, a phase when tumor cells and immunity enter into a dynamic equilibrium and the tumor expansion is arrested; D20 represents the escape phase, in which progressively growing tumors appear, and solid tumors form.

To evaluate the early detection capability of IRdye800-M-HFn nanoprobes, we injected the tumor-bearing mice (n=4 for each time point) through the tail vein with IRdye800-M-HFn nanoprobes on D4, D11, and D20, respectively. Consecutively, NIR-FMI was performed on each mouse before and 4 h after injection. The signal of the HFn-based nanoprobe was observed in the tumor inoculation area on D4, disappeared on D11, and re-appeared on D20 (Figure 3C), and these results correlate with the BL signals of tumor cells. To further investigate the specificity of IRdye800-M-HFn nanoprobes, we performed NIR-FMI of normal tissues and tumors *ex vivo*. Results on the signals of IRdye800-M-HFn nanoprobes in tumor tissues on D4, D11, and D20 (Figure 3D) were similar when compared with those from *in vivo* NIR-FMI at the corresponding times. Furthermore, the nanoprobes showed high signals in the liver and kidney, the main organs for ferritin nanoprobe metabolism, which was consistent with the findings of previous reports (Liang et al., 2014; Zhao et al., 2016). The *in vivo* and *ex vivo* NIR-FMI images post-injection demonstrated the visualization of

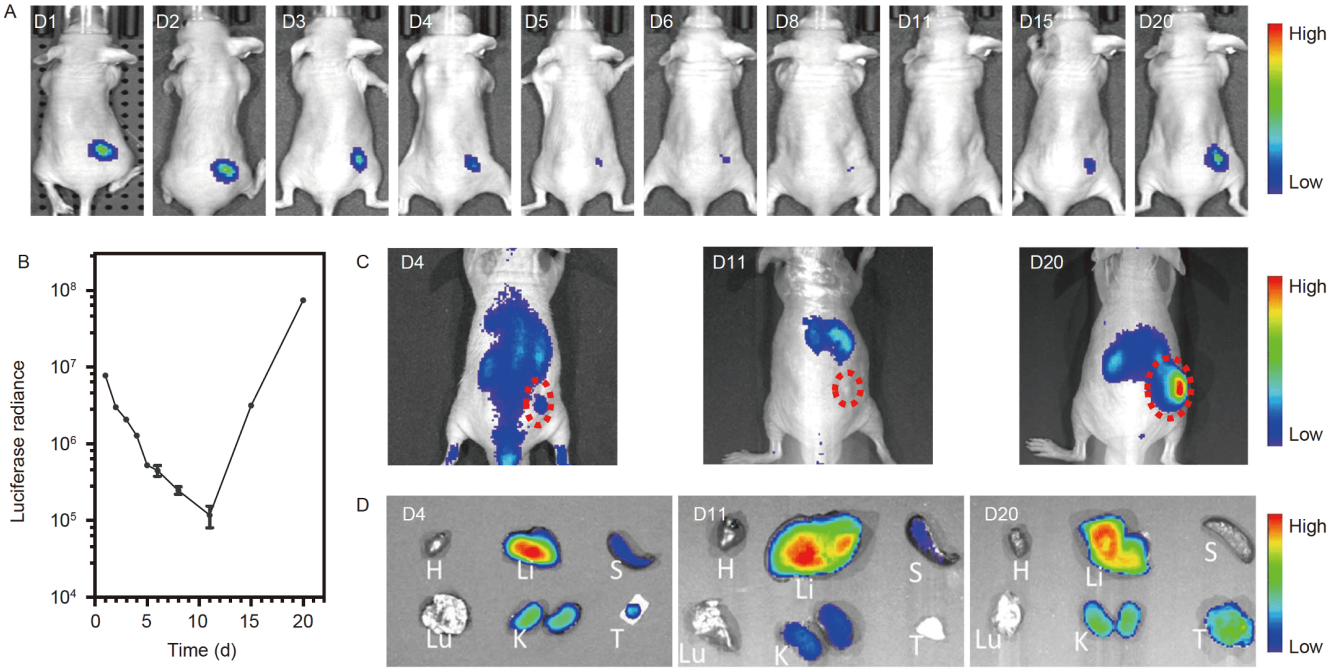

Figure 3 *In vivo* NIR-FMI images of HepG2 tumor xenografted mice using IRdye800-M-HFn nanoprobes. A, BL imaging of HepG2 tumor cells at different time points after implantation in mice. B, Quantitative analysis of BL imaging signal of implanted tumor cells *in vivo*, n=3. C, NIR-FMI of HepG2 tumor cells *in vivo* at different time points. The red circles indicate the tumor inoculation area. D, *Ex vivo* imaging of tumors and normal tissues. The tissues were arranged in the following order: heart (H), liver (Li), spleen (S), lung (Lu), kidney (K), and tumor (T). Tumor tissues (with a part of skin tissues) on D4 and D11.

tumor cells (D4) before they formed solid tumor tissues (Figure 3C and D). No fluorescence signal was detected in the tumor tissues on D11, whereas a significant signal was detected on D20. To explore how early the IRdye800-M-HFn nanoprobes can detect tumor cells, we further performed NIR-FMI on D2, D3 (before D4), and D8 (between D4 and D11). Unexpectedly, the results showed that the NIR-FMI signals on D2 and D3 were clearly visualized by IRdye800-M-HFn nanoprobes (Figure S3 in Supporting Information). These results further confirmed that HFn-based nanoprobes can specifically target implanted HepG2 tumor cells at the pre-solid tumor stage.

In vivo PAI and MRI of tumor cells by IRdye800-M-HFn at the pre-solid tumor stage

To verify the NIR-FMI result, we further employed PAI and MRI techniques to image the tumor cells using HFn-based nanoprobes. The PAI and MRI images were co-registered with the NIR-FMI images, showing consistency between the three modalities (Figure 4A–C). For PAI, the signal before and after the tail-vein injection on D4, D11, and D20 exhibited similar results compared with those obtained by NIR-FMI. By acquiring T_2-weighted magnetic resonance images, we were able to compare the results between before and after the injection on D4, D11, and D20. A region-of-interest quantification of the signals in the implanted tumors showed a significant increase in the photoacoustic signals and a decrease in the MRI signals compared with those before the tail-vein injection on D4 and D20. However, no significant changes were observed on D11 (Figure 4D and E). The photoacoustic signals increased by 100% on D4, exhibited nearly no difference on D11, and increased by 200% on D20. The MRI contrast-to-noise ratio decreased by 20% on D4, showed nearly no change on D11, and decreased by 40% on D20. The PAI and MRI signals on D4 and D20 revealed significant differences from those on D11 (Figure 4D and E). Prussian blue staining further confirmed the presence of IRdye800-M-HFn in D4 tumor tissues, but slight staining was observed in D11 tumor tissues (Figure S4 in Supporting Information).

We next sought to determine the mechanism of M-HFn nanoprobes in targeting tumor cells at the early stage via the blood circulation system. We employed PAI, which provides high-resolution functional information of hemoglobin and blood oxygenation, to visualize the oxyhemoglobin distribution in the tumor area. A significant amount of blood hemoglobin around the implanted tumor cells was observed on D4 but not on D11 (Figure 4F). The histopathological analysis of the tissue sections also showed blood vessels surrounding the implanted tumor cells on D4 but not on D11 (Figure S5 in Supporting Information). On D20, abundant blood hemoglobin was shown in the region of the xenograft tumor tissue (Figure 4F). These data indicate that there were blood vessels surrounding the tumor cells at the early stages before solid tumor formation. The triple-modality HFn nanoprobes possibly penetrated into the tumor cell area from the blood vessels, specifically targeting tumor cells and internalizing them via TfR1-mediated endocytosis. On D11, most of the tumor cells were dead, and no blood vessels were

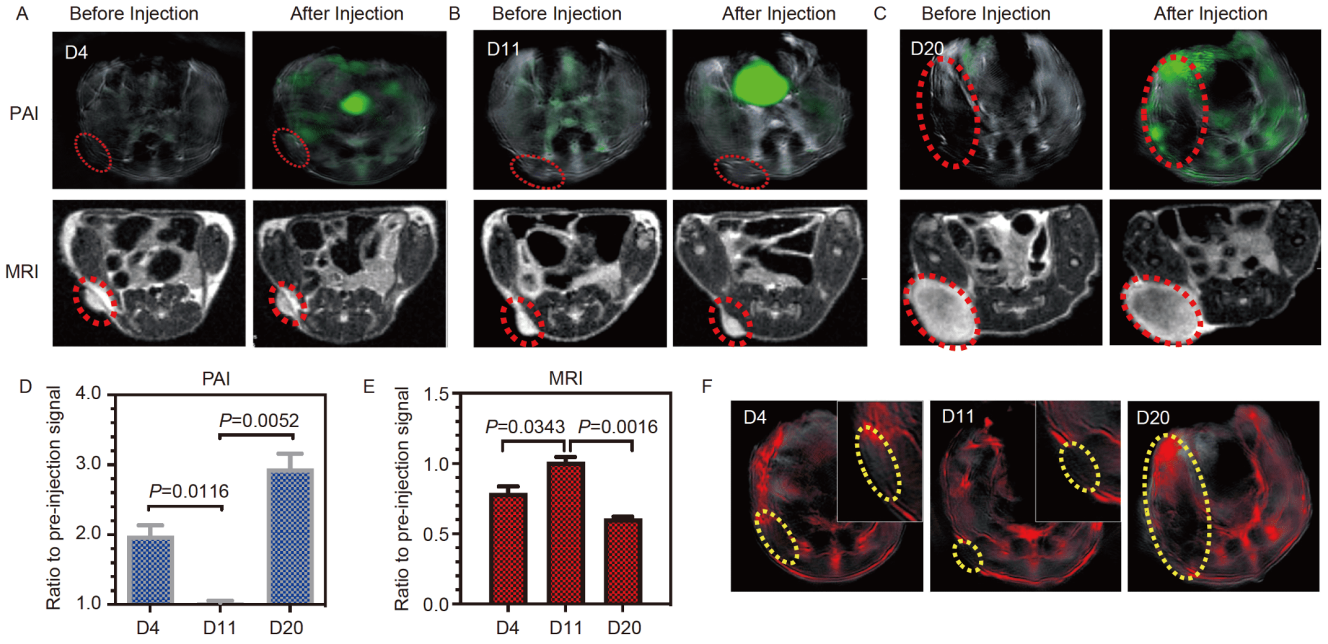

Figure 4 *In vivo* PAI and MRI of HCC tumor cells in live mice using IRdye800-M-HFn nanoprobes. A–C, PAI and MRI were performed at 4 (A), 11 (B), and 20 d (C) after HepG2 tumor cells were implanted in mice. D and E, Quantitative analyses of PAI (D) and MRI (E) at the tumor region. F, PAI analyses of oxyhemoglobin saturation in the tumor regions at different times. The red and yellow circles indicate the tumor areas.

shown to have contact with the surviving tumor cells. Thus, no nanoprobe signal was observed. After solid tumor tissues formed, new tumor blood vessels were generated by tumor angiogenesis, and the HFn nanoprobes can once again target tumor tissues via the EPR effect and active TfR1 tumor-targeting mechanism.

HFn-Dox effectively killed xenograft HepG2 tumors at the early stage

The above NIR-FMI, PAI, and MRI data of nanoprobes confirmed the effective accumulation of HFn nanoprobes in the area of implanted tumor cells. The excellent targeting capability of HFn nanoprobes for pre-solid tumor cells ensures HFn nanocarrier a potential early-stage tumor therapy agent. Next, we prepared HFn-doxorubicin (Dox) for early-stage tumor therapy by loading the first-line chemotherapeutic agent Dox into the cavity of HFn nanocarriers (Figure 5A). As previously reported, using a channel-based drug loading strategy, we encapsulated more than 100 Dox molecules into an HFn nanocage under 60°C heat treatment (Jiang et al., 2020).

To test the therapeutic effect of HFn-Dox on early-stage tumors, we first subcutaneously injected HepG2 cells into BALB/c nude mice. Then, HFn-Dox was intravenously injected into the mice at 5 mg kg^{-1} Dox equivalents on D3 and D7 (Figure 5B). We also administered free Dox (5 mg kg^{-1}), HFn, and phosphate-buffered saline (PBS) as controls. Although the tumor from the control groups (free Dox, HFn, and PBS) grew rapidly and reached above 1,000 mm^3 on D44, the tumor growth was significantly inhibited after injection of HFn-Dox twice (**, $P<0.01$, unpaired *t*-test) (Figure 5C). Moreover, the HFn-Dox-treated mice showed no evident body weight loss when compared with the PBS group during the experimental period (Figure 5D). All the mice from the HFn-Dox group remained alive on D58; 83.3% of the mice from the HFn-Dox group were alive on D65, whereas the survival period of mice from free Dox, HFn, and PBS groups was shorter than 50 d (Figure 5E). Owing to the specific tumor-targeting capability of HFn as early as two days after the tumor cells were implanted, HFn-Dox can effectively kill tumor cells at the early tumor stage.

HFn-Dox effectively killed metastatic tumor cells at the early HCC-lung-metastasis stage

Owing to the therapeutic effect of HFn-Dox on the pre-formation of solid tumors, we hypothesized that HFn-Dox might be used to block the formation of tumor metastases. When tumor metastasis occurs, tumor cells are intravasated into nearby blood or lymphatic vessels, followed by the escape of cancer cells from the lumina of such vessels into the parenchyma of distant tissues; then, small nodules of cancer cells form, and they finally grow into macroscopic tumors (Hanahan and Weinberg, 2011). Given that the lung is the most easily affected organ during extrahepatic metastases (Uchino et al., 2011), we constructed a HepG2-Luc early-lung-metastasis mouse model to mimic the early HCC-lung-metastasis stage(Headley et al., 2016) within a certain period during the circulation of HCC cells, which started seeding in the lung but showed no evident tumor nodule formation (Figure 5F). We intravenously injected HepG2-Luc tumor cells into BALB/c nude mice on D0 and monitored the *in vivo* fluorescein signal in the lung area of mice every day. On D5, we discovered a feeble fluorescein signal generated from the HepG2-Luc cells in the lung area of mice, which indicated that HepG2-Luc cells were seeded in the lung tissue. These tumor cells were at the early-lung-metastasis stage as proven by the hematoxylin and eosin (HE) staining of paraffin-embedded lung slices from HepG2-Luc lung metastasis mice on D5 (Figure 5G). Fluorescein isothiocyanate (FITC)-HFn-based fluorescence staining of these continuous lung slices further confirmed that HFn specifically targets tumor cells at the early-lung-metastasis stage (Figure 5G). The anti-CD45 antibody-based fluorescence staining of these continuous lung slices showed that a large number of CD45-positive inflammatory cells infiltrated around these tumor cells (Figure 5G).

To further test the therapeutic effect of HFn-Dox on early HCC-lung-metastasis stage tumors, we intravenously injected HFn-Dox into mice at 10 mg kg^{-1} Dox equivalents on D5 and D10 (Figure 5F). Free Dox (10 mg kg^{-1}), HFn, and PBS were also administered as controls. The therapeutic effect was monitored by examining the BL signals generated from the HepG2-Luc cells (Figure 5H and I). After two times of administrations, mice from the HFn-Dox group showed a significantly reduced tumor growth compared with those given free Dox, HFn, and PBS (Figure 5H and I). These results indicated that HFn-Dox could target tumor cells at the early metastasis stage and realize early metastasis tumor therapy.

Inflammation-mediated blood vessel leakage enabled HFn to target tumors at the early stage

The above results confirmed the potential of multimodality ferritin nanocages for early theranostics of tumors. Given that no new tumor blood vessels were generated at the early stage of implanted tumor cells, how HFn nanoprobes reached the tumor area and specifically targeted tumor cells remained unanswered. We hypothesized that the formation of the tumor microenvironment provided a mechanism for HFn nanoprobes to pass through the endothelial barrier of vascular vessels and further target tumor cells. Platelets can guide the formation of early-tumor microenvironment niches by rapidly recruiting granulocytes to tumor cells, causing an increase in the permeability of endothelial cells (Labelle et al., 2014). Blood clotting mediated by platelets was observed in

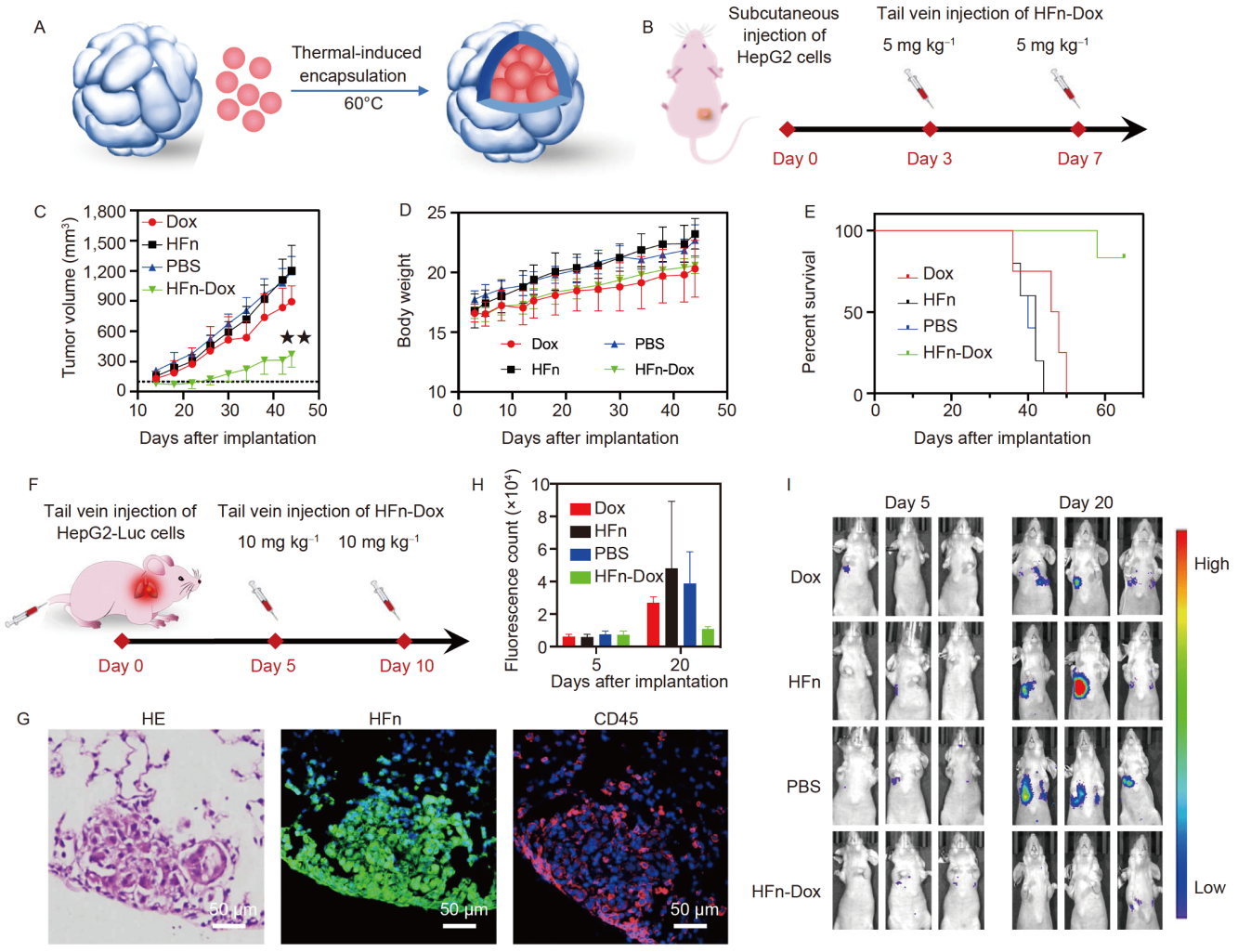

Figure 5 HFn-Dox for early tumor therapy. A, Dox was encapsulated into the ferritin nanocage at 60°C. B, Schematic of HepG2 xenograft model in the early therapy experiment. C–E, HepG2 tumor cells were implanted subcutaneously into mice on D0. Mice were intravenously administered with HFn-Dox or Dox (5 mg kg^{-1} Dox equivalents, n=5) on D3 and D7, and HFn and PBS were administered as controls. C, Tumor volume of each treated group. **, P<0.01, unpaired t-test. D, Bodyweight change during different treatments. E, Survival curves under different treatments. F, Schematic of therapy experiment with HepG2-Luc early-lung-metastasis model. G, HE staining (left), FITC-HFn-based fluorescence staining (middle), and 555-anti CD45 antibody-based fluorescence staining (right) of paraffin-embedded lung slices from mice with early-lung-metastasis tumors of HCC. (Scale bar=50 μm). H and I, *In vivo* BL imaging and statistical fluorescein signal analysis of HepG2-Luc early-lung-metastasis in mice that were injected with HFn-Dox (10 mg kg^{-1} Dox equivalents, n=5) on D5 and D10, Dox (5 mg kg^{-1}, n=5) on D5 and D10, and HFn and PBS administered as controls.

the tumor-infiltrated tissues on D4 (Figure S5 in Supporting Information), indicating the increased permeability of endothelial cells. The inflammation of implanted sites can further promote the formation of the tumor environment (Ben-Neriah and Karin, 2011), in which the process can increase the permeability of blood vessels and facilitate the penetration of macrophages or monocytes into the tumor area (Ben-Neriah and Karin, 2011; Coussens and Werb, 2002). In the immunohistochemical staining of CD11b, the marker of myeloid cells, the xenograft HCC tumor tissue sections of D4, indicated the abundant myeloid cells, which infiltrated from blood vessels to implanted tumor cell areas on D4 (Figure S6 in Supporting Information). Moreover, a large number of CD45-positive leukocyte cells infiltrated around metastasis HCC tumor cells in the paraffin-embedded lung slices from HepG2-Luc lung metastasis mice on D5 (Figure 5G). Considering the above data, we believe that the HFn nanoprobes, which are notably smaller than leukocyte cells, with a size close to that of the reported serum proteins, can pass through the endothelial gaps in the inflammation site. Thus, in this period, HFn nanoprobes can also accumulate in the tumor sites. The specific targeting property of HFn to TfR1-positive HCC cells allowed HFn-based nanoprobes to effectively accumulate in tumor cells. Moreover, we observed the absence of HFn nanoprobe accumulation in the inflammation site induced by lipopolysaccharide without tumor cells (Figure S7 in Supporting Information), which further confirmed the specificity of HFn nanoprobes to tumors. Altogether, the tumor-associated inflammation-mediated blood vessel leakage enables HFn to target tumors at the

early stage (Figure S8 in Supporting Information).

CONCLUSIONS

In conclusion, we have developed a triple-modality nanoprobe by using engineered ferritin nanoparticle labeled with IRdye800 on the protein shell for NIR-FMI and PAI while encapsulating a superparamagnetic iron oxide core for MRI. Combining the unique targeting property and proper size of ferritin nanoprobe, we achieved for the first time TfR1-riched HCC tumor imaging at the early stage before solid tissue formation via tumor-associated inflammation-mediated blood vessel leakage. NIR-FMI, PAI, and MRI ensured the accuracy of early tumor detection. Our findings may extend the diagnostic capability earlier than that can be achieved at the moment, which potentially increases the chance for a successful treatment. The tumor-associated inflammation-mediated blood vessel leakage effect along with tumorigenesis may be an ideal window to exploit the detection capabilities of nanoprobes for early-stage tumor cells.

Moreover, taking advantage of the unique architecture of HFn, a great number of chemotherapeutic drugs have been encapsulated into the ferritin nanocage (Fan et al., 2013; Jiang et al., 2020; Liang et al., 2014). Here, we demonstrated that by loading Dox into the cavity of HFn nanocages, the HFn-Dox drug delivery system showed high efficiency in eliminating early-stage tumor cells. Thus, HFn nanoprobes can also be potentially used for early-stage tumor therapy. In addition, for the first time, we demonstrated that besides albumin and coagulation factors, as a serum protein, ferritin can pass through the endothelial barrier via inflammation-mediated blood vessel leakage, which can expand the application of ferritin-based nanoprobes in inflammation-related disease and may benefit the study of the physiological and pathological functions of ferritin.

In our HepG2-Luc early-lung-metastasis mouse model, the process of lung metastasis tumor formation following intravenous tumor cell injection is similar to that of tumor loading during metastatic tumor cell seeding (Headley et al., 2016). Studying tumor cells before the formation of solid tissues will help us better understand the mechanisms of tumor invasion and metastasis. Altogether, this work provides a promising early-stage tumor detection and therapy and a strategy to better understand the relationship between tumor microenvironment and formation.

MATERIALS AND METHODS

HFn protein biosynthesis and purification

HFn was produced in accordance with the descriptions of our previous reports (Fan et al., 2012; Liang et al., 2014). Briefly, the expression vector HFn-pET-30a(+) was transformed into *E. coli* BL21 (DE3) (TransGen Biotech, Beijing, China) following the manufacturer's instructions. HFn-pET-30a-BL21 *E. coli* cells were cultured overnight at 37°C in LB medium with 50 mg L^{-1} kanamycin. Then, 0.75 mmol L^{-1} isopropyl-β-D-thiogalactoside (Sigma-Aldrich, USA) was added in the medium, and *E. coli* cells were cultured for an additional 8 h at 30°C. Then, the HFn-pET-30a-BL21 *E. coli* cells were harvested by centrifugation at 4,000×*g* for 30 min at 4°C, and the pellets were re-suspended in Tris buffer (20 mmol L^{-1} Tris, pH 8.0). The re-suspended HFn-pET-30a-BL21 *E. coli* cells were broken by the high-pressure homogenizer (Scientz-150, Ningbo, China) at 4°C and centrifuged at 10,000×*g* for 30 min at 4°C to separate the supernatants. The supernatant was heated at 72°C for 15 min to denature most of the *E. coli* proteins. After centrifugation at 10,000×*g* for 30 min at 4°C, ammonium sulfate (520 g L^{-1}) was added in the supernatant to precipitate HFn protein. The precipitate was collected by centrifugation at 10,000×*g* for 30 min at 4°C and then dissolved in Tris buffer (20 mmol L^{-1} Tris, pH 8.0). After dialyzing out ammonium sulfate in Tris buffer (20 mmol L^{-1} Tris, pH 8.0), the HFn protein was purified by anion-exchange chromatography on a Q-Sepharose Fast Flow column (GE Healthcare, Sweden) and size-exclusion chromatography on a superdex^{TM} 200 pg column (GE Healthcare). The concentration of HFn was determined in triplicate by the BCA protein assay kit (Pierce, USA) using bovine serum albumin (BSA) as the standard. The typical yield of HFn was 100 mg per 1 L patch.

Preparation of M-HFn nanoparticles

HFn protein shells were used as the reaction template to synthesize iron oxide nanoparticles, following the method reported by Fan et al. (2012). Briefly, a degassed solution of HFn protein (0.25 mg mL^{-1} in 100 mmol L^{-1} NaCl) was added to a jacketed reaction vessel under N_2. The temperature of the reaction vessel was kept at 65°C, and the pH was titrated to 8.5. Ammonium iron(II) sulfate hexahydrate $(NH_4)_2Fe(SO_4)_2{\cdot}6H_2O$ was added as an iron source at a rate of 100 Fe/(protein min) to attain a theoretical loading factor of 5,000 Fe molecules per protein. Simultaneously, the freshly prepared H_2O_2 was added at a stoichiometric equivalent of 1:3 H_2O_2:Fe^{2+} as an oxidant. The reaction was considered complete 5 min after the addition of iron and H_2O_2. Sodium citrate was added to chelate any free iron. The synthesized M-HFn nanoparticles were centrifuged to remove aggregated nanoparticles and dialyzed against PBS overnight. The concentration of M-HFn nanoparticles was assumed to be the same as that of HFn protein and determined using a BCA protein assay kit (Pierce, Thermo Fisher Scientific, USA). Purified M-HFn nanoparticles were obtained with a yield of >90%.

Labeling and characterization of M-HFn nanoparticles

The IRdye800-M-HFn nanoprobes were prepared by conjugating IRdye800-NHS ester (LI-COR, Inc., USA) onto the surface lysine of HFn protein shell, in accordance with the instructions of commercial kits. Briefly, 100 nmol L^{-1} IRdye800-NHS ester in 5 μL dimethyl sulfoxide (Sigma-Aldrich) was added to 50 M-HFn solutions in 1 mL PBS buffer. The mixture was incubated at 4°C overnight with gentle shaking. The raw products were then passed through a PD MiniTrap G-25 column (GE Healthcare) to remove the unreacted IRdye800 molecules. The dye concentration of IRdye800-M-HFn was determined by UV-Vis spectroscopy (Nanodrop 2000, Thermo Fisher Scientific). The protein concentration was measured by the BCA protein assay kit (Pierce) using BSA as the standard. Typically, the IRdye800: M-HFn molecule ratio in the final products was about 13:1.

The prepared IRdye800-M-HFn nanoparticles were characterized using Cryo-EM (FEI Titan Krios 300kV, FEI, USA) and TEM (Tecnai F20, FEI), as previously reported (Fan et al., 2012). The size distribution of iron oxide core was measured by Image J software (NIH) and analyzed by GraphPad Prism 6.02 (GraphPad Software).

The preparation of FITC-HFn and FITC-M-HFn was performed following the instructions of commercial kits. In brief, 200 nmol L^{-1} FITC isomer I (Sigma-Aldrich) was added to 50 nmol L^{-1} HFn or M-HFn solution in 1 mL carbonate/bicarbonate buffer (100 mmol L^{-1} carbonate, pH 9.0). The mixture was incubated at room temperature for 1 h. The mixture was purified with a PD MiniTrap G-25 column (GE Healthcare). The FITC-conjugated HFn or M-HFn was concentrated, and the buffer was replaced with PBS in a Vivaspin-4 Centrifugal Concentrator (MWCO 100 kD, Sartorius, Germany). The concentrations of FITC and HFn protein of FITC-HFn were determined in the same way as IRdye 800-HFn. The final ratio of FITC:HFn molecules in the product FITC-HFn was about 11:1. The labeling ratio of FITC:M-HFn was similar to that of FITC-HFn.

Cell-binding assays

The binding activities of HFn and M-HFn nanoparticles to HepG2 cells were determined on a FACSCalibur (Becton Dickinson, USA) flow cytometry system. We incubated 100 μL detached HepG2 cell suspensions (2.5×10^5 cells) with 0.4 μmol L^{-1} of FITC-HFn or FITC-M-HFn in PBS containing 0.5% BSA on ice for 45 min. Then the cells was washed in cold PBS for three times and analyzed immediately with a FACSCalibur flow cytometry system. FITC-conjugated BSA was used as a negative control.

The binding affinities of M-HFn nanoparticles to TfR1 on HepG2 cells were determined using a saturation binding assay in accordance with our previous report (Fan et al., 2012). Briefly, 2.5×10^5 HepG2 cells were incubated with increasing concentrations (10^{-12} to 10^{-7} mol L^{-1}) of FITC-M-HFn. After incubation, the cells were washed three times in cold PBS and collected. Cell-bound fluorescence was measured by FACSCalibur flow cytometry system. The dissociation constant (K_d) was calculated using GraphPad Prism 6.02 (GraphPad Software). Experiments were performed on quadruplicate samples.

Cellular culture

The human HCC cell lines HepG2 and HepG2-Luc, the human breast cancer cell line MX-1 were obtained from the Institute of Basic Medical Sciences, Chinese Academy of Medical Sciences. The HepG2 and HepG2-Luc cells were cultured in Dulbecco's Modified Eagle Medium (Gibco, Thermo Fisher Scientific) containing 10% fetal calf serum (Gibco) at 37°C with 5% CO_2. The MX-1 cells were cultured in DMEM/F12 GlutaMAX Medium (Gibco) containing 10% fetal calf serum (Gibco) at 37°C with 5% CO_2.

NIR-FMI

All *ex vivo* and *in vivo* NIR-FMI experiments were conducted with an IVIS Spectrum imaging system (PerkinElmer, USA). We adopted a black 96-well plate to measure the fluorescent signals of probes at different concentrations. For *in vivo* imaging, the tumor mouse models were scanned at pre-injection and 4 h post tail-vein injection of the probes right after PAI. A filter set with excitation and emission wavelengths of 745 and 800 nm, respectively, was used to acquire fluorescent signals. Imaging data were processed and analyzed by IVIS Living Image 3.0 software (PerkinElmer).

MRI

We conducted *ex vivo* MRI scans of the probes with a 7-T superconducting magnet system (BioSpec 70/20 USR, Bruker, Germany). We obtained the T_2-weighted scans of probes at various concentrations with echo time (TE)/repetition time (TR)=100/3,100 ms. Relaxivity r_2 was measured and calculated from the slope of relaxation times (T_2) versus the concentrations of HFn nanoprobe. For *in vivo* MRI scans, we used small-animal compact MRI systems (Aspect Imaging, Israel). We acquired the MRI data of tumor mouse models at the time points, pre-injection and 4 h post tail-vein injection right after fluorescence imaging. The TE and TR parameters were the same as those of *ex vivo* experiments with a slice thickness of 1 mm.

PAI

All phantoms and *in vivo* PAI experiments were conducted

using an inVision 128 small animal imaging system (iThera Medical GmbH, Germany). The system consists of a tunable laser with working wavelengths ranging from 680 to 960 nm. The light pulses excited photoacoustic signals and were further acquired by using a multi-element cylindrically-focused ultrasound transducer. The phantom comprised polyurethane with two cylindrical spaces inside for the measurement of photoacoustic signals of the probes. One space was filled with PBS and the other with probes of a certain concentration. The experimental animals were anaesthetized with 1.6% isoflurane inhalant delivered in 0.8 L of medical air and 0.1 L of oxygen. The mice were mounted on an animal holder with a thin plastic membrane to avoid the direct touch of the water in an imaging chamber under isoflurane anesthesia. Images were scanned with a step distance of 0.5 mm. We performed scanning 10 times at each moving step for averaging. Six excitation wavelengths (715, 730, 760, 773, 800, and 850 nm) were used to generate multispectral photoacoustic information. The tumor mouse models were scanned from the liver to lower limbs during pre-injection and 4 h after the injection of probes. The acquired data were reconstructed using the multispectral processing along with ViewMSOT software (iThera Medical GmbH). We used multispectral analyses to unmix the signals of oxygen hemoglobin, dioxygen hemoglobin, and the probes for more information.

Histological staining assays

On D4 and D11, mice were sacrificed at 4 h post-injection. Tumor tissues were collected, fixed, and embedded in paraffin sections for subsequent staining.

For the immunohistochemical staining assay, the paraffin-embedded tumor tissue sections were deparaffinized twice in xylene for 10 min and then hydrated progressively with an ethanol gradient. The endogenous peroxidase activity was blocked by incubation with freshly prepared 0.3% H_2O_2 in methanol for 30 min. After rinsing in PBS buffer for three times, the tissue sections were incubated in citrate buffer (10 mmol L^{-1}, pH 6.0) at 100°C for 30 min for antigen retrieval. Then, nonspecific antigens were blocked with 5% goat serum in PBS for 1 h at 37°C. Tissue sections were then incubated with different molecular marker antibodies, including TfR1—1:50 dilution of mouse anti-human TfR1 monoclonal antibody (Abcam, Clone 10F11, UK), CD11b—1:100 dilution of rabbit anti-mouse CD11b monoclonal antibody (Abcam, Clone EPR1344) and CD45—1:100 dilution of rabbit polyclonal to CD45 (Abcam, Clone 10558), at 37°C for 1 h. After rinsing in PBS three times, the tissue sections were incubated with a 1:200 dilution of HRP conjugated goat anti-mouse (for TfR1) or goat anti-rabbit antibody (for CD11b and CD45) at 37°C for 45 min. The visualization of positive tissues was achieved by a diaminobenzidine system. Then, the tissue sections were counterstained with hematoxylin (blue stain). Following staining, the sections were dehydrated through graded alcohols to xylene and sealed with resin.

For the Prussian blue staining assay, the tumor tissues were stained by a Perls stain kit (Solarbio, Beijing, China) and then washed with PBS for three times. The tissues were also counterstained with HE staining. The images were acquired by microscopy (Leica, Germany).

Preparation of HFn-Dox

The preparation of HFn-Dox was performed in accordance with the descriptions of our previous work (Jiang et al., 2020). HFn protein at 2 mg mL^{-1} was mixed with 7.5 mg Dox in 10 mL 20 mmol L^{-1} Tris-HCl buffer (pH 8.0). The mixture was then incubated at 60°C for 4 h with a gentle rotation and then centrifugated at 10,000×*g* for 10 min to separate the supernatant. Then, the free Dox was removed from the supernatant by HiPrep^{TM} 26/10 desalting column to obtain the purified HFn-Dox complex in PBS buffer.

Animal experiments

All animal studies were performed following the protocol approved by the Chinese Academy of Sciences Institutional Animal Care and Use Committee. Female BALB/c nude mice (6–8 weeks old) were purchased from SPF (Beijing) Biotechnology Co., Ltd.

To establish the subcutaneous transplanted HepG2 tumor model, we subcutaneously implanted the BALB/c nude mice with 1×10^6 HepG2 tumor cells in the right upper flank. The mice were randomly divided into four groups (n=5 mice in each group) and administered with HFn-Dox or Dox (5 mg kg^{-1} Dox equivalents, n=5) via the tail vein on D3 and D7 after the transplantation. HFn and PBS were administered as controls. The body weight and tumor volume of the mice were measured every other day. Tumor volume was calculated by $L\times W^2/2$, where L and W represent the maximum and minimum tumor diameter, respectively.

To establish the HepG2-Luc early-lung-metastasis mouse model, we intravenously injected 6–8-week-old female BALB/c nude mice with 2×10^6 HepG2-Luc tumor cells. Then, the IVIS Spectrum imaging system (PerkinElmer) was used to monitor the BL signals generated from HepG2-Luc cells every day after transplantation. On D5 after tumor cell transplantation, the tumor cell signals were detected.

Compliance and ethics *The author(s) declare that they have no conflict of interest.*

Acknowledgements *This work was supported by the National Natural Science Foundation of China (31900981, 62027901, and 32000996), the Strategic Priority Research Program of CAS (XDB29040101), CAS Inter-*

disciplinary Innovation Team (JCTD-2020-08), Chinese Academy of Sciences (YJKYYQ20180048), the Key Research Program of Frontier Sciences, CAS (QYZDY-SSW-SMC013), the National Key Research and Development Program of China (2017YFA0205501, 2017YFA0205200), Youth Innovation Promotion Association of Chinese Academy of Sciences (2019093), China Postdoctoral Science Foundation (2020M682358), the China Postdoctoral Science Special Foundation (2020TQ0280), the Grant for International Joint Research Project of the Institute of Medical Science, the University of Tokyo (Extension-2019-K3005), the Beijing-Tianjin-Hebei Basic Research Cooperation Special Program (19JCZDJC65300), and the CAS Key Laboratory of Mental Health Grant (KLMH2020K02). We thank Dr.s Xiaojun Huang and Gang Ji for their excellent technical support in cryo-EM imaging at the Transmission EM Facilities, Center for Biological Imaging, Institute of Biophysics. We also thank Jingnan Liang for technical support in TEM imaging at the Core Facility of Equipment, Institute of Microbiology. We thank Prof.s Shuaidong Huo and João Conde for their beneficial discussions and comments on our manuscript.

References

Alexiou, A., Vairaktarakis, C., Tsiamis, V., and Ashraf, G.M. (2015). Application of efficient nanoparticles for early diagnosis and treatment of cancer. Curr Drug Metab 16, 662–675.

Ben-Neriah, Y., and Karin, M. (2011). Inflammation meets cancer, with NF-κB as the matchmaker. Nat Immunol 12, 715–723.

Chinen, A.B., Guan, C.M., Ferrer, J.R., Barnaby, S.N., Merkel, T.J., and Mirkin, C.A. (2015). Nanoparticle probes for the detection of cancer biomarkers, cells, and tissues by fluorescence. Chem Rev 115, 10530–10574.

Coussens, L.M., and Werb, Z. (2002). Inflammation and cancer. Nature 420, 860–867.

Croci, D.O., Cerliani, J.P., Dalotto-Moreno, T., Méndez-Huergo, S.P., Mascanfroni, I.D., Dergan-Dylon, S., Toscano, M.A., Caramelo, J.J., García-Vallejo, J.J., Ouyang, J., et al. (2014). Glycosylation-dependent lectin-receptor interactions preserve angiogenesis in anti-VEGF refractory tumors. Cell 156, 744–758.

Daniels, T.R., Delgado, T., Helguera, G., and Penichet, M.L. (2006a). The transferrin receptor part II: targeted delivery of therapeutic agents into cancer cells. Clin Immunol 121, 159–176.

Daniels, T.R., Delgado, T., Rodriguez, J.A., Helguera, G., and Penichet, M. L. (2006b). The transferrin receptor part I: Biology and targeting with cytotoxic antibodies for the treatment of cancer. Clin Immunol 121, 144–158.

Falvo, E., Tremante, E., Fraioli, R., Leonetti, C., Zamparelli, C., Boffi, A., Morea, V., Ceci, P., and Giacomini, P. (2013). Antibody–drug conjugates: targeting melanoma with cisplatin encapsulated in protein-cage nanoparticles based on human ferritin. Nanoscale 5, 12278–12285.

Fan, K., Cao, C., Pan, Y., Lu, D., Yang, D., Feng, J., Song, L., Liang, M., and Yan, X. (2012). Magnetoferritin nanoparticles for targeting and visualizing tumour tissues. Nat Nanotech 7, 459–464.

Fan, K., Gao, L., and Yan, X. (2013). Human ferritin for tumor detection and therapy. WIREs Nanomed Nanobiotechnol 5, 287–298.

Fan, K., Jia, X., Zhou, M., Wang, K., Conde, J., He, J., Tian, J., and Yan, X. (2018). Ferritin nanocarrier traverses the blood brain barrier and kills Glioma. ACS Nano 12, 4105–4115.

Fan, K., Zhou, M., and Yan, X. (2017). Questions about horse spleen ferritin crossing the blood brain barrier via mouse transferrin receptor 1. Protein Cell 8, 788–790.

Feng, M., Gao, W., Wang, R., Chen, W., Man, Y.G., Figg, W.D., Wang, X. W., Dimitrov, D.S., and Ho, M. (2013). Therapeutically targeting glypican-3 via a conformation-specific single-domain antibody in hepatocellular carcinoma. Proc Natl Acad Sci USA 110, E1083–E1091.

Frangioni, J.V. (2008). New technologies for human cancer imaging. J Clin Oncol 26, 4012–4021.

Greish, K. (2010). Enhanced permeability and retention (EPR) effect for anticancer nanomedicine drug targeting. In: Grobmyer, S., and Moudgil, B., eds. Cancer Nanotechnology. Methods in Molecular Biology (Methods and Protocols). New York: Humana Press. 25–37.

Hanahan, D., and Weinberg, R.A. (2011). Hallmarks of cancer: the next generation. Cell 144, 646–674.

He, J., Fan, K., and Yan, X. (2019). Ferritin Drug Carrier (FDC) for tumor targeting therapy. J Control Release 311-312, 288–300.

Headley, M.B., Bins, A., Nip, A., Roberts, E.W., Looney, M.R., Gerard, A., and Krummel, M.F. (2016). Visualization of immediate immune responses to pioneer metastatic cells in the lung. Nature 531, 513–517.

Hopkins, C.R. (1983). Intracellular routing of transferrin and transferrin receptors in epidermoid carcinoma A431 cells. Cell 35, 321–330.

Jiang, B., Chen, X., Sun, G., Chen, X., Yin, Y., Jin, Y., Mi, Q., Ma, L., Yang, Y., Yan, X., et al. (2020). A natural drug entry channel in the ferritin nanocage. Nano Today 35, 100948.

Jiang, B., Yan, L., Zhang, J., Zhou, M., Shi, G., Tian, X., Fan, K., Hao, C., and Yan, X. (2019a). Biomineralization synthesis of the cobalt nanozyme in SP94-ferritin nanocages for prognostic diagnosis of hepatocellular carcinoma. ACS Appl Mater Interfaces 11, 9747–9755.

Jiang, B., Zhang, R., Zhang, J., Hou, Y., Chen, X., Zhou, M., Tian, X., Hao, C., Fan, K., and Yan, X. (2019b). GRP78-targeted ferritin nanocaged ultra-high dose of doxorubicin for hepatocellular carcinoma therapy. Theranostics 9, 2167–2182.

Kircher, M.F., de la Zerda, A., Jokerst, J.V., Zavaleta, C.L., Kempen, P.J., Mittra, E., Pitter, K., Huang, R., Campos, C., Habte, F., et al. (2012). A brain tumor molecular imaging strategy using a new triple-modality MRI-photoacoustic-Raman nanoparticle. Nat Med 18, 829–834.

Labelle, M., Begum, S., and Hynes, R.O. (2014). Platelets guide the formation of early metastatic niches. Proc Natl Acad Sci USA 111, E3053–E3061.

Li, L., Fang, C.J., Ryan, J.C., Niemi, E.C., Lebrón, J.A., Björkman, P.J., Arase, H., Torti, F.M., Torti, S.V., Nakamura, M.C., et al. (2010). Binding and uptake of H-ferritin are mediated by human transferrin receptor-1. Proc Natl Acad Sci USA 107, 3505–3510.

Li, X., Qiu, L., Zhu, P., Tao, X., Imanaka, T., Zhao, J., Huang, Y., Tu, Y., and Cao, X. (2012). Epidermal growth factor-ferritin H-chain protein nanoparticles for tumor active targeting. Small 8, 2505–2514.

Liang, M., Fan, K., Zhou, M., Duan, D., Zheng, J., Yang, D., Feng, J., and Yan, X. (2014). H-ferritin-nanocaged doxorubicin nanoparticles specifically target and kill tumors with a single-dose injection. Proc Natl Acad Sci USA 111, 14900–14905.

Lima, L.G., and Monteiro, R.Q. (2013). Activation of blood coagulation in cancer: implications for tumour progression. Biosci Rep 33.

Maru, Y. (2016). Inflammation and Metastasis. Tokyo: Springer Japan.

Peng, D., Du, Y., Shi, Y., Mao, D., Jia, X., Li, H., Zhu, Y., Wang, K., and Tian, J. (2016). Precise diagnosis in different scenarios using photoacoustic and fluorescence imaging with dual-modality nanoparticles. Nanoscale 8, 14480–14488.

Smith, R.A., Cokkinides, V., and Eyre, H.J. (2006). American Cancer Society guidelines for the early detection of cancer, 2006. CA Cancer J Clin 56, 11–25.

Sun, T., Zhang, Y.S., Pang, B., Hyun, D.C., Yang, M., and Xia, Y. (2014). Engineered nanoparticles for drug delivery in cancer therapy. Angew Chem Int Ed 53, 12320–12364.

Swann, J.B., and Smyth, M.J. (2007). Immune surveillance of tumors. J Clin Invest 117, 1137–1146.

Teicher, B.A. (2006). Tumor models for efficacy determination. Mol Cancer Ther 5, 2435–2443.

Thorsen, F., Fite, B., Mahakian, L.M., Seo, J.W., Qin, S., Harrison, V., Johnson, S., Ingham, E., Caskey, C., Sundstrøm, T., et al. (2013). Multimodal imaging enables early detection and characterization of changes in tumor permeability of brain metastases. J Control Release 172, 812–822.

Uchida, M., Flenniken, M.L., Allen, M., Willits, D.A., Crowley, B.E., Brumfield, S., Willis, A.F., Jackiw, L., Jutila, M., Young, M.J., et al. (2006). Targeting of cancer cells with ferrimagnetic ferritin cage nanoparticles. J Am Chem Soc 128, 16626–16633.

Uchida, M., Terashima, M., Cunningham, C.H., Suzuki, Y., Willits, D.A., Willis, A.F., Yang, P.C., Tsao, P.S., McConnell, M.V., Young, M.J., et al. (2008). A human ferritin iron oxide nano-composite magnetic resonance contrast agent. Magn Reson Med 60, 1073–1081.

Uchino, K., Tateishi, R., Shiina, S., Kanda, M., Masuzaki, R., Kondo, Y., Goto, T., Omata, M., Yoshida, H., and Koike, K. (2011). Hepatocellular carcinoma with extrahepatic metastasis. Cancer 117, 4475–4483.

Wang, W., Knovich, M.A., Coffman, L.G., Torti, F.M., and Torti, S.V. (2010). Serum ferritin: Past, present and future. Biochim Biophys Acta 1800, 760–769.

Wang, Z., Zhang, S., Zhang, R., Chen, X., Sun, G., Zhou, M., Han, Q., Zhang, B., Zhao, Y., Jiang, B., et al. (2021). Bioengineered dual-targeting protein nanocage for stereoscopical loading of synergistic hydrophilic/hydrophobic drugs to enhance anticancer efficacy. Adv Funct Mater 31, 2102004.

Xing, Y., Zhao, J., Conti, P.S., and Chen, K. (2014). Radiolabeled nanoparticles for multimodality tumor imaging. Theranostics 4, 290–306.

Zhang, Y., Li, Y., Zhang, J., Chen, X., Zhang, R., Sun, G., Jiang, B., Fan, K., Li, Z., and Yan, X. (2021). Nanocage-based capture-detection system for the clinical diagnosis of autoimmune disease. Small 17, 2101655.

Zhao, Y., Liang, M., Li, X., Fan, K., Xiao, J., Li, Y., Shi, H., Wang, F., Choi, H.S., Cheng, D., et al. (2016). Bioengineered magnetoferritin nanoprobes for single-dose nuclear-magnetic resonance tumor imaging. ACS Nano 10, 4184–4191.

SUPPORTING INFORMATION

The supporting information is available online at https://doi.org/10.1007/s11427-021-1976-0. The supporting materials are published as submitted, without typesetting or editing. The responsibility for scientific accuracy and content remains entirely with the authors.